HHS Public Access

Author manuscript

Nat Neurosci. Author manuscript; available in PMC 2017 July 09.

Published in final edited form as:

Nat Neurosci. 2017 February ; 20(2): 219–229. doi:10.1038/nn.4471.

Modulation of excitation on parvalbumin interneurons by neuroligin-3 regulates the hippocampal network

Jai S. Polepalli[1], **Hemmings Wu**[2], **Debanjan Goswami**[1], **Casey H. Halpern**[2], **Thomas C. Südhof**[3,4], and **Robert C. Malenka**[1]

[1]Nancy Pritzker Laboratory, Department of Psychiatry and Behavioral Sciences, Stanford University School of Medicine, Stanford, CA 94305

[2]Department of Neurosurgery, Stanford University School of Medicine, Stanford, CA 94305

[3]Department of Molecular and Cellular Physiology, Stanford University School of Medicine, Stanford, CA 94305

[4]Howard Hughes Medical Institute, Stanford University School of Medicine, Stanford, CA 94305

Abstract

Hippocampal network activity is generated by a complex interplay between excitatory pyramidal cells and inhibitory interneurons. Although much is known about the molecular properties of excitatory synapses on pyramidal cells, comparatively little is known about excitatory synapses on interneurons. Here, we show that conditional deletion of the postsynaptic cell adhesion molecule neuroligin-3 in parvalbumin interneurons causes a decrease in NMDA receptor-mediated postsynaptic currents and an increase in presynaptic glutamate release probability due to selectively impairing the inhibition of glutamate release by presynaptic Group III metabotropic glutamate receptors. As a result, the neuroligin-3 deletion altered network activity by reducing gamma oscillations and sharp wave ripples; changes associated with a decrease in extinction of contextual fear memories. These results demonstrate that neuroligin-3 specifies the properties of excitatory synapses on parvalbumin-containing interneurons by a retrograde trans-synaptic mechanism and suggest a novel molecular pathway whereby neuroligin-3 mutations contribute to neuropsychiatric disorders.

Optimal neural circuit function is critical for effective information processing that mediates cognitive processes and is dependent on the specification of the precise properties of individual synapses. Synapses in the forebrain initially form in excess but are subsequently pruned, strengthened and eliminated in an experience-dependent manner. This process gives

Correspondence to: R. Malenka, Dept. of Psychiatry and Behavioral Sciences, Stanford University School of Medicine, 265 Campus Drive, Room G1021, Stanford, CA 94305-5453, 650-724-2730, 650-498-4585, malenka@stanford.edu.

AUTHOR CONTRIBUTIONS

J.S.P., T.C.S. and R.C.M. conceived the project, designed the experiments and wrote and edited the manuscript. H.W performed the *in vivo* electrophysiology experiments with input from C.H.H. and D.G. performed the immunohistochemistry experiments.

COMPETING FINANCIAL INTERESTS

The authors declare no competing financial interests.

rise to functional neuronal ensembles that enable computations critical for precise information processing. In the hippocampus, circuits computing contextual and spatiotemporal information involve glutamatergic pyramidal cells and various types of GABAergic interneurons, which play critical roles in the information processing underlying learning and memory via, in part, the generation of functionally important neural oscillations[1–3]. The critical importance of interneurons in optimal circuit performance is emphasized by recent suggestions that a range of prominent neuropsychiatric disorders involve abnormalities in the functioning of GABAergic interneurons[4].

Although both excitatory and inhibitory cells in hippocampal ensembles are driven to spike by glutamatergic excitatory synapses, most of our understanding of the molecular specification of synaptic properties comes from study of excitatory synapses on principal glutamatergic cells. In contrast, the molecular architecture underlying excitatory synapses on GABAergic interneurons, which are biophysically and structurally different from excitatory synapses on principal neurons[5–7], and in turn transform the incoming excitation into various forms of inhibition, is poorly understood. To more comprehensively elucidate the molecular architecture of excitatory synapses on GABAergic interneurons, here we focus on the role of the postsynaptic cell adhesion protein neuroligin-3 (NL3) in specifying the properties of excitatory synapses on parvalbumin (PV) interneurons in the CA1 region of the hippocampus.

NL3 is of particular interest because of its known genetic association with a variety of neuropsychiatric disorders, notably autism[8,9]. Moreover, the availability of NL3 conditional knockout mice, which have been used previously to advance our understanding of its role in circuit function and repetitive behaviors[10], facilitates analysis of its cell-type specific functions. NL3 belongs to the neuroligin family of synaptic cell-adhesion molecules (NL1–4), which are differentially expressed at excitatory and inhibitory synapses[9], with NL1 and NL2 localized to excitatory and inhibitory synapses, respectively. Although NL3 is present at both excitatory and inhibitory synapses, its detailed functions at excitatory synapses in general and at excitatory synapses on GABAergic interneurons specifically have yet to be established.

Here we report that genetic deletion of postsynaptic NL3 from PV interneurons in the CA1 region of the hippocampus enhances presynaptic glutamate release via specific loss of functioning of presynaptic Group III mGluRs, which normally mediate tonic inhibition of glutamate release on PV interneurons. Combined with a decrease in NMDA receptor (NMDAR)-mediated postsynaptic responses due to the NL3 deletion, this presynaptic modulation results in a frequency-dependent change of net circuit function as evidenced by a decrease in the frequency of network oscillations in the gamma (35–85 Hz) and sharp wave ripple (SWR) range (100–200 Hz). Behavioral assays reveal that the NL3 deletion from hippocampal CA1 PV interneurons specifically impaired contextual fear extinction without altering fear conditioning itself. Thus, NL3 confers specific properties to excitatory synapses on hippocampal CA1 PV GABAergic interneurons, which importantly contribute to the role of these interneurons in controlling hippocampal network activity and hippocampal-dependent behavioral functions.

RESULTS

Postsynaptic effects of conditional KO of NL3 from CA1 PV interneurons

We deleted NL3 specifically from PV interneurons by crossing homozygous female conditional NL3 knockout mice ($NL3^{fl}$)[10] with male mice that have been engineered to drive cre recombinase under the parvalbumin promoter (PV-cre) (Jackson Laboratories; stock number 08069). Since NL3 is located on the X chromosome, breeding homozygous floxed NL3 ($NL3^{fl}$) female mice to homozygous PV-cre male mice produced male offspring which carry a PV specific deletion of NL3 ($NL3^{fl}$/PV-Cre) (Supplementary Fig. 1a). We previously confirmed the deletion of NL3 in $NL3^{fl}$ mice by performing qPCR on $NL3^{fl}$/Nestin-Cre mice, which showed a complete absence of NL3 while levels of NL1 and NL2 were unaltered[10]. Histological examination of the forebrain in $NL3^{fl}$/PV-Cre mice did not reveal any difference in the density or distribution of PV cells in the hippocampal formation (Supplementary Fig. 1b,c) or in the frontal cortex (data not shown), ruling out the possibility of an early disruption of PV cell development.

To examine the electrophysiological consequences of deleting NL3 from PV interneurons in the hippocampus, we stereotactically injected postnatal 21 day old PV-Cre and $NL3^{fl}$/PV-Cre mice with an AAV virus encoding eGFP in a double inverse open reading frame (DIO) driven by the human synapsin promoter (AAV-hSyn-DIO-eGFP) (Supplementary Fig. 2a). After 10–14 days, acute hippocampal slices were prepared and whole cell recordings were made from eGFP expressing PV cells in the stratum oriens of the hippocampus (Supplementary Fig. 2b). Current clamp recordings revealed that deletion of NL3 did not detectably alter the basic membrane properties of PV interneurons as assayed by spike frequency in response to a twice threshold depolarizing pulse (Fig. 1a), resting membrane potential (Fig. 1b) or the magnitude of the afterhyperpolarization potential (Fig. 1c). Neither the amplitude nor frequency of AMPA receptor (AMPAR)-mediated miniature excitatory postsynaptic currents (mEPSC) were affected by NL3 deletion from PV interneurons (Fig. 1d, e). There also was no change in the amplitude or frequency of $GABA_A$ receptor-mediated miniature inhibitory postsynaptic currents (mIPSCs) (Supplementary Fig. 3).

AMPAR EPSCs in PV interneurons display robust inward rectification and fast decay kinetics because a high proportion of the synaptic AMPARs in PV interneurons lack GluA2 subunits[11]. However, deletion of NL3 from PV cells did not significantly influence the rectification properties or decay kinetics of AMPAR EPSCs (Fig. 1f). Given that synaptic AMPAR function and number appear unaltered following NL3 deletion from PV interneurons and NMDARs are variably expressed in these cells[12], we next assayed NMDA receptor (NMDAR)-mediated synaptic transmission using NMDAR EPSC to AMPAR EPSC ratios. NL3 deletion caused an ~60% reduction in NMDAR/AMPAR ratios (Fig. 1g) without causing any changes in NMDAR stoichiometry or biophysical properties as assayed by the rise time, decay time constants, and current-voltage relationships of pharmacologically isolated NMDAR EPSCs (Fig. 1h–j). Additionally, examining the density of synapses on PV neurons by staining for PSD-95 and the AMPAR subunit GluA4 on the dendrites of PV-Cre and NL3fl/PV-Cre neurons revealed no significant effect of NL3 deletion (Fig. 1k–m), assayed as the number of PSD-95 puncta per dendritic length (Fig. 1l) or the proportion of

PSD-95 puncta containing detectable GluA4 (Fig. 1m). Thus, the NL3 deletion in CA1 PV interneurons caused a reduction in postsynaptic NMDAR-mediated synaptic transmission without detectable changes in the postsynaptic properties of either AMPAR- or $GABA_A$R-mediated synaptic currents nor excitatory synapse density.

Presynaptic effects of conditional KO of NL3 from CA1 PV interneurons

As a further test for effects of the NL3 KO in PV interneurons on basal synaptic transmission, we examined the input-output (I-O) relationship of AMPAR EPSCs at incremental stimulus intensities and, surprisingly, observed a significant increase in EPSC amplitudes in $NL3^{fl}$/PV-Cre cells as a function of stimulus strength (Fig. 2a). We then measured paired-pulse ratios (PPRs) at multiple interstimulus intervals, a measure that inversely correlates with presynaptic release probability[13] and found that postsynaptic deletion of NL3 from PV interneurons caused a clear decrease in PPRs (Fig. 2b), indicative of an increase in glutamate release probability. At central synapses, different presynaptic machinery may mediate spontaneous release in the absence of action potentials (i.e. mEPSCs recorded in the presence of tetrodotoxin) and action potential-dependent evoked/spontaneous EPSCs[14]. Given that we did not see a change in mEPSC properties in these cells (Fig. 1d, e), we examined if spontaneous EPSCc (sEPSCs) are altered in $NL3^{fl}$/PV-Cre cells. Deletion of postsynaptic NL3 caused an increase in the frequency of sEPSCs without any significant change in their amplitude (Fig. 2c, d), findings that are consistent with the observed decrease in PPRs. To test if these changes in I-O relationship, PPRs and sEPSC do indeed indicate a change in presynaptic release probability, we examined the rate of block of pharmacologically isolated NMDAR EPSCs by MK-801, a measure that directly correlates with release probability[15]. Consistent with the change in PPRs and sEPSC frequency caused by NL3 deletion, the block of NMDAR EPSCs by MK-801 was accelerated in $NL3^{fl}$/PV-Cre cells (Fig. 2e, f). Thus three different electrophysiological measures of evoked presynaptic release probability are all consistent with the hypothesis that NL3 deletion from PV interneurons increases the release probability at excitatory synapses on these neurons.

Recent studies demonstrated that genetic deletion of NL3 from CA1 pyramidal cells or their presynaptic partners neurexins can influence the tonic release of endocannabinoids (eCBs) and the consequent activity of presynaptic CB1 receptors, thereby influencing transmitter release[16,17]. To determine whether a similar mechanism occurs at excitatory synapses on PV interneurons, we applied the CB1 receptor agonist WIN55212-2. The application of WIN55212-2 elicited comparable reductions in EPSCs and increases in the PPR in PV-Cre and $NL3^{fl}$/PV-Cre cells (Fig. 3a–d, Supplementary Fig. 4ai, aii), confirming the presence of CB1 receptors on excitatory presynaptic terminals on PV interneurons[18]. To determine whether tonic eCB release influences these synapses, we applied the CB1 receptor antagonist AM251 but observed no effect on EPSCs or PPRs in PV-Cre or $NL3^{fl}$/PV-Cre interneurons (Fig. 3e–h, Supplementary Fig. 4bi, bii). Thus a reduction in tonic activation of presynaptic CB1 receptors cannot account for the increase in glutamate release probability caused by NL3 deletion in PV interneurons.

Transmitter release at forebrain synapses is regulated by a variety of presynaptic receptors including autoreceptors[19]. Because presynaptic terminals on hippocampal interneurons are

selectively enriched in Group III metabotropic glutamate receptors (Group III mGluRs)[20], we next applied the Group III mGluR agonist, L-AP4. In PV-Cre neurons, L-AP4 application caused an ~40% decrease in EPSC amplitudes with an accompanying increase in the PPR. Strikingly, L-AP4 had no significant effect in $NL3^{fl}$/PV-Cre cells (Fig. 3i–l, Supplementary Fig. 4ci, cii). Similarly, the Group III mGluR antagonist LY-341495 caused ~2-fold increase in EPSC amplitude in PV-Cre interneurons with an accompanying decrease in the PPR but had no significant effect in $NL3^{fl}$/PV-Cre cells (Fig. 3m–p, Supplementary Fig. 4di, dii). These results indicate that excitatory synapses on PV interneurons are inhibited by tonic activation of presynaptic Group III mGluRs and that this modulation is absent following the genetic deletion of NL3. The effects of the postsynaptic NL3 deletion on presynaptic receptor function at these synapses appeared to be specific for mGluRs because the depression of EPSCs caused by the $GABA_B$ receptor agonist baclofen (Supplementary Fig. 4ei, eii; Supplementary Fig. 5a–d) or the A_1 adenosine receptor agonist N^6-CPA (Supplementary Fig. 4fi, fii; Supplementary Fig. 5e–h) was not altered by the NL3 deletion. Thus, postsynaptic deletion of NL3 from PV interneurons specifically impaired the presynaptic inhibition of glutamate release by Group III mGluRs but had no effect on the presynaptic modulation mediated by CB1 receptors, $GABA_B$ receptors or A_1 adenosine receptors.

Network effects of the NL3 deletion from CA1 PV interneurons

To begin to elucidate the network effects of the NL3 deletion from PV interneurons, we examined the effects of repetitive activation of excitatory synapses at a wide range of frequencies (20 stimuli at 2–200 Hz) including those that occur during various forms of hippocampal oscillatory activity, such as in theta, gamma and ripple frequencies[1,2, 21–25]. To avoid inducing postsynaptic plasticity during these trains, we added the calcium chelator BAPTA (10 mM) to the pipette solution. At moderate frequencies (2–10 Hz), the facilitation of EPSCs during the train in PV-Cre interneurons was modest and not dramatically affected by the NL3 deletion (Fig. 4a, Supplementary Fig. 6a). At 20–50 Hz, an impairment of the train-induced facilitation by NL3 deletion became more apparent, while at 100 Hz and 200 Hz, the difference between PV-Cre and $NL3^{fl}$/PV-Cre cells was dramatic (Fig. 4a,b, Supplementary Fig. 6a,b). Furthermore, during repetitive activation of excitatory synapses in current clamp configuration, spikes were reliably generated in both PV-cre and $NL3^{fl}$/PV-Cre cells at a low frequency (5 Hz) (Fig. 4c) but spiking was significantly attenuated at a high frequency (100 Hz) in PV cells lacking NL3 (Fig. 4d). This frequency-dependent attenuation in information transfer (i.e. EPSC amplitudes and spiking probability) in $NL3^{fl}$/PV-Cre interneurons suggests that these cells now function as low pass filters in that they reliably integrate information (i.e. EPSCs) at lower frequencies but not at higher frequencies (Supplementary Fig. 6c).

The dramatic reduction in facilitation of EPSCs and spiking during high frequency stimulation in PV interneurons lacking NL3 would be expected to have an effect on the net inhibition generated in CA1 pyramidal cells during high frequency trains. To test this hypothesis, we made current clamp recordings from CA1 pyramidal cells in the absence of GABA receptor antagonists during a 50 Hz train (Fig. 4e). In wild-type slices, by the 4^{th} stimulus IPSPs appear to shunt EPSP summation giving rise to a plateau effect during which

EPSP amplitude stabilizes at ~4 fold its initial amplitude (Fig. 4f–i). In NL3^{fl}/PV-Cre slices, EPSPs in CA1 pyramidal cells summate supralinearly during the early phase of the stimulus train, as indicated by an increase in the slope of the synaptic summation, and the much larger EPSP summation (~6 fold) during the latter half of the train (Fig. 4h, i), presumably due to a decrease in PV interneuron mediated inhibition at this frequency.

Given that PV interneurons control the excitation of principal cells and thus gate network activity, we next examined the effects of NL3 deletion from PV interneurons on hippocampal circuit function by making *in vivo* recordings from freely behaving PV-cre and NL3^{fl}/PV-Cre mice implanted with a linear four channel recording electrode in the CA1 region (Supplementary Fig. 7a). The power spectra of the local field potentials (LFPs) in the theta oscillation range (3–12 Hz) were not significantly altered in NL3^{fl}/PV-Cre mice (3–12 Hz) (Fig. 5a–c), with only a left shift in the peak theta frequency in NL3^{fl}/PV-Cre mice (peak theta frequency: 6.0 ± 0.6 Hz in PV-Cre mice; 4.0 ± 0.5 in NL3^{fl}/PV-Cre mice). In contrast, LFP power spectra at higher frequency oscillations including gamma (35–85 Hz) were reduced by ~60% in NL3^{fl}/PV-Cre mice (Fig 5c). This resulted in a ~70% reduction in the gamma to theta ratio in NL3^{fl}/PV-Cre mice (Supplementary Fig. 7b). We also examined the power spectrum, amplitude and frequency of individual sharp wave ripple oscillations (SWR) during immobility. Similar to gamma oscillations, the power spectrum of the isolated SWRs was dramatically decreased in NL3^{fl}/PV-Cre mice (Fig. 5d–f) due to a ~70% decrease in the amplitude of the SWR (Fig. 5g, Supplementary Fig. 7c) and a ~50% decrease in the length of the SWR (Fig. 5h). However, the rate of SWRs was not significantly affected (Fig. 5i).

We also examined SWRs in acute hippocampal slices, a preparation in which changes in afferent activity to the hippocampus due to the NL3 deletion from PV interneurons in brain regions other than the hippocampus cannot influence acute hippocampal oscillatory activity. Application of a high potassium solution reliably induced SWRs[25] (Fig. 5j), which qualitatively exhibited similar effects of deletion of NL3 from PV interneurons as the SWRs recorded *in vivo* (Fig. 5k–o). Specifically, slices from NL3^{fl}/PV-Cre mice exhibited lower power in the 100–200 Hz range (Fig. 5k,l), a decrease in SWR length (Fig. 5n), and a decrease in SWR rate (Fig. 5o) but no detectable change in SWR amplitude (Fig. 5m). Thus, deletion of NL3 from PV neurons causes a decrease in hippocampal gamma oscillations and SWRs, patterns of activity which have been implicated in various phases of hippocampal-dependent learning and memory[3,23,24].

Behavioral effects of the NL3 deletion from hippocampal PV interneurons

Since the synaptic changes caused by the NL3 deletion in PV interneurons modulated hippocampal circuit activity in a manner that might be expected to influence hippocampal-dependent memory functions, we investigated if PV interneurons are critical for hippocampal dependent learning and memory processes as previously suggested[3, 26]. In an initial set of experiments, we expressed in these neurons hM4Di, an inhibitory designer receptor exclusively activated by a designer drug (DREADD), using stereotaxic injection of an appropriate cre-dependent AAV (AAV-hSyn-DIO-hM4Di-mCherry) into the hippocampus of PV-cre mice. Mice were exposed to a hippocampal-dependent contextual

fear conditioning task, during which mice learned to associate a neutral context with an aversive foot shock and the learned fear was measured by freezing behavior[27] (Fig. 6a). Experimental mice were injected with the hM4Di agonist clozapine-N-oxide (CNO) twice a day on both conditioning day 1 and extinction days 2–5. Control PV-cre mice expressing GFP and hM4Di-expressing mice showed virtually identical freezing behavior during both the baseline habituation session and the 3 conditioning sessions. However, hM4Di-expressing mice displayed much less extinction of freezing when the footshock no longer occurred (Fig. 6b). Thus inhibition of CA1 PV interneurons did not influence the acquisition of conditioned fear but significantly impaired its extinction.

To investigate the role of NL3 in PV interneurons in mediating this behavior, we tested $NL3^{fl}$/PV-Cre mice using this protocol. The behavioral results were essentially identical to those observed when PV interneurons were inhibited by the DREADD. The NL3 KO in PV interneurons had no effect on learning to associate the context with the footshock as assessed by freezing behavior, but the retention of fear on day 2 was higher in $NL3^{fl}$/PV-Cre mice and the extinction of context-induced freezing was significantly reduced (Fig. 6c). To determine if loss of NL3 specifically in CA1 PV interneurons was responsible for the impairment in extinction, we expressed full length NL3 in the hippocampal PV interneurons of $NL3^{fl}$/PV-Cre mice by injecting AAV virus encoding NL3 in a double inverse open reading frame (AAV-hSyn-DIO-NL3-t2a-Venus) 3–4 weeks prior to the behavioral experiments. Histological examination revealed a ~90% co-localization for NL3-Venus and parvalbumin in hippocampal PV interneurons through the dorsal-ventral axis (Supplementary Fig 8a–c). This hippocampal PV interneuron-specific rescue manipulation rescued contextual fear extinction in $NL3^{fl}$/PV-Cre mice while having no effect on conditioned freezing (Fig. 6d).

To test if the rescue of the extinction deficit due to NL3 deletion from PV neurons is associated with rescue of the synaptic changes caused by this genetic manipulation, we made recordings from $NL3^{fl}$/PV-Cre cells expressing the full length NL3. These cells exhibited NMDAR/AMPAR ratios (Supplementary Fig. 9a) and PPRs (Supplementary Fig 9b) that were the same as those recorded from control PV neurons as well as a normal reduction in EPSC amplitude due to application of the Gr-III mGluR agonist L-AP4 (Supplementary Fig 9c–e). Thus the major synaptic changes caused by NL3 deletion from PV neurons were rescued by expression of NL3 in young adult hippocampus.

To examine if other forms of hippocampal-dependent learning might be disrupted in $NL3^{fl}$/PV-Cre mice, we subjected these mice to a reward alternation task in a T maze. In this assay, both PV-Cre and $NL3^{fl}$/PV-Cre mice performed at chance on day 1 and learned the task at similar rates during days 2–7 (Supplementary Fig. 10a). The $NL3^{fl}$/PV-Cre mice also did not exhibit any atypical motor behaviors as assayed by total distance travelled (Supplementary Fig. 10b), low motion bouts (Supplementary Fig. 10c) or stereotypy (Supplementary Fig. 10d), all measured on a force plate actometer[28]. Thus deletion of NL3 from PV interneurons in the hippocampus specifically affected extinction of conditioned fear likely due to its complex modification of excitatory synaptic drive, which in turn influenced hippocampal network activity.

DISCUSSION

Using a cell-restricted conditional KO approach, we have defined a critical role for the postsynaptic cell-adhesion molecule NL3 in controlling the properties of excitatory synapses on PV interneurons in the CA1 region of the hippocampus. Moreover, we demonstrate that changes in synaptic excitation to hippocampal PV interneurons modify hippocampal circuit properties, specifically the frequency of gamma oscillations and SWRs, and presumably as a consequence of these changes in network properties modify the extinction of conditioned fear. Given that NL3 deletions and point mutations are genetically associated with ASDs[8, 9], it is plausible to suggest that the abnormalities described here contribute to some of the cognitive symptoms manifested by these prominent disorders. In contrast, distinct cell type- and circuit-specific changes due to the NL3 deletion cause abnormalities in other behavioral domains such as repetitive motor routines[10], thus emphasizing the daunting complexity of defining even how a “simple” single genetic manipulation influences circuit function and behavior.

Our electrophysiological characterization of genetically labelled CA1 PV interneurons revealed two surprising changes at excitatory synapses due to the NL3 deletion; a decrease in NMDAR-mediated synaptic responses and an increase in presynaptic release probability, both of which could be rescued by selectively replacing NL3 in $NL3^{fl}$/PV-Cre cells. While in other cell types in hippocampus, striatum and amygdala NL1 appears to be required to maintain normal NMDAR-mediated synaptic transmission[29–31], our findings suggest that in CA1 PV interneurons NL3 fulfills this role and that NL1 does not compensate for the loss of NL3.

The mechanism by which the NL3 deletion enhances glutamate release is more surprising. In CA1 pyramidal cells, the NL3 deletion enhances GABA release at a subset of inhibitory synapses due to disruption of tonic endocannabinoid signaling[16]. In marked contrast, we demonstrate here that tonic inhibition of glutamate release at excitatory synapses on CA1 PV interneurons is not mediated by endocannabinoids but instead by Group III mGluRs and that this mGluR-mediated inhibition is eliminated by NL3 deletion. This presynaptic consequence of the postsynaptic NL3 deletion is specific in that the effects of other prominent presynaptic neuromodulators were unaffected. Furthermore, mIPSCs were unaffected by NL3 deletion from CA1 PV interneurons, in marked contrast to the robust decrease in mIPSCs caused by its deletion from nucleus accumbens D1 medium spiny neurons[10]. Together these results suggest that postsynaptic NL3 in hippocampal PV neurons is required for the normal function and/or recruitment of presynaptic Group III mGluRs, which are selectively enriched at synaptic terminals on hippocampal interneurons[20, 32–38].

The autoreceptor activity of group III mGluRs appears to be critical for maintaining sustained release of glutamate at stimulation frequencies above ~50 Hz as evidenced by the finding that following the NL3 deletion, EPSCs and synaptically evoked spikes show a marked attenuation with successive stimuli (Fig. 4b, d). As a consequence of this decrease in excitatory drive onto CA1 PV interneurons at these frequencies, postsynaptic potentials (PSP) in CA1 pyramidal neurons exhibited supralinear summation (Fig. 4e–i). Because normal PV interneuron function is required for the generation of oscillatory network activity

including gamma oscillations and SWRs[2, 39, 40], we suggest that the observed decrease in gamma oscillations and SWRs (Fig. 5) due to the deletion of NL3 in these neurons is due to a net decrease in their activity at high frequencies and the consequent reduction in circuit-level inhibition.

SWRs play a critical role in hippocampal-dependent learning and consolidation of recently formed memories[3,23,24]. Although the decrease in SWRs due to the deletion of NL3 from PV interneurons did not influence the development of contextual fear conditioning nor learning of a spatial reward alternation task, extinction of conditioned fear was dramatically impaired. Importantly, by performing cell type-restricted expression of inhibitory DREADDs and local Cre-dependent NL3 rescue experiments, we demonstrated that this impairment was in fact due to dysfunctions specifically in hippocampal PV interneurons. Although we did not include CNO or vehicle treated mice as controls for the DREADD experiments, the lack of change in baseline freezing and fear conditioning itself after CNO injections in the DREADD mice suggests that any stress caused by the injection does not account for the observed impairment of fear extinction. Deleting the requisite NMDAR subunit GluN1 from PV interneurons caused more dramatic effects than NL3 deletion in various learning and memory assays[3, 41]. However, in this previous work, experiments were not performed to directly test whether these deficits were solely due to deficits in hippocampal PV interneuron function.

In summary, we have shown that deletion of NL3 from CA1 PV interneurons causes changes at excitatory synapses unlike those observed at any of the distinct synapses studied to date. These findings emphasize that the function of individual synaptic proteins often depends on the specific molecular architecture in which they are embedded. This appears to be particularly the case for the neuroligin/neurexin family of synaptic cell-adhesion proteins[9,10,16,17,42,43]. Furthermore, combined with previous work on NLs[10, 29,44–47] our findings emphasize the challenges and importance of defining the specific synapses and circuits that are responsible for the behavioral abnormalities caused by manipulations of proteins that are genetically associated with brain disorders.

ONLINE METHODS

Generation of NL3^{fl}/PV-Cre mice

NL3^{fl}/PV-Cre were generated by crossing homozygous female conditional NL3 knockout mice (cNL3 KO)[10] with homozygous male mice that have been engineered to drive cre recombinase under the parvalbumin promoter (PV-cre). Age matched male PV-cre mice, generated by crossing homozygous PV-cre male mice with female PV-cre mice were used as controls in all experiments.

In vivo injections

Postnatal 18–21 day old PV-Cre and NL3^{fl}/PV-Cre mice were prepared for stereotaxic injection using standard procedures approved by the Stanford University Administrative Panel on Laboratory Animal Care. Briefly, animals were anesthetized with a mixture of ketamine (75 mg/kg body weight) and dexmedetomidine (0.375 mg/kg body weight) by

intraperitoneal injection. Following immobilization on a Kopf stereotaxic apparatus, mice were injected bilaterally with AAV virus containing one of hSyn-DIO-eGFP, hSyn-DIO-hM4Di-mCherry or hSyn-DIO-NL3-t2a-Venus[10]. For electrophysiological experiments virus was injected at coordinates −1.8 mm posterior, −1.5 mm lateral to bregma at a depth of 1.3–1.4 mm from the dura to target the hippocampus. For behavioral experiments in 2–3 month old mice, virus was injected at 4 sites on each hemisphere at coordinates −1.8 and −2.1mm posterior, −1.4 and −1.8 mm lateral to bregma at a depth of 1.4–1.7 mm from the dura to target the entire hippocampus. Viral solution (1 μl) in a glass cannula was injected using a microinjection pump (Harvard Apparatus) at a flow rate of 0.1 μl/min in each hemisphere sequentially. The scalp was sealed with cyanoacrylate and atipamezole was injected (10 mg/kg body weight i.p.) to reverse the effect of dexmedetomidine.

Slice electrophysiology

Ten to fifteen days following the injection of AAV virus, animals were anesthetized with halothane and the brains rapidly removed and placed in ice-cold, high sucrose cutting solution containing (in mM): 228 sucrose, 26 $NaHCO_3$, 11 glucose, 2.5 KCl, 1 NaH_2PO_4, 7 $MgSO_4$ and 0.5 $CaCl_2$. 300 μm sections were cut on a Leica vibratome in the high sucrose cutting solution, and immediately transferred to an incubation chamber containing artificial cerebrospinal fluid (ACSF) containing (in mM) 119 NaCl, 26 $NaHCO_3$, 11 glucose, 2.5 KCl, 1 NaH_2PO_4, 1.3 $MgSO_4$ and 2.5 $CaCl_2$. The slices were allowed to recover at 32°C for 30 min before being allowed to equilibriate at room temperature for a further 1 h. During recordings, the slices were placed in a recording chamber constantly perfused with heated ACSF (28–30°C) and gassed continuously with 95% O_2 and 5% CO_2. For voltage clamp recordings, borosilicate glass pipettes (3–5 MΩ) were filled with an internal solution containing (in mM) 135 $CsMeSO_4$, 8 NaCl, 10 HEPES, 0.25 EGTA, 2 Mg_2ATP, 0.3 Na_3GTP, 0.1 spermine and 7 phosphocreatine (pH 7.25–7.3; osmolarity 294–298). Data was collected with a MultiClamp 700B amplifier (Axon Instruments) and digitized at 8 kHz using an ITC-18 A/D converter (Instrutech Corporation) and filtered at 4 KHz. Data were acquired and analyzed using Axograph-X (Axograph).

PV interneurons were identified by the presence of GFP on an upright microscope (Olympus BX51WI, Olympus Optical) and visualized by infrared differential interference contrast. mEPSCs were recorded at −60 mV in the presence of 100 μm picrotoxin, 50 μm AP-5 and 0.1 μM TTX. For mIPSCs, picrotoxin was replaced by 20 μM NBQX. A theta glass pipette filled with ACSF was used as a bipolar stimulation electrode and was placed in the CA1 oriens-alveus layer to evoke EPSCs in PV cells. Cells were held at −60 or −70 mV to record AMPAR EPSCs while stimulating afferent inputs at 0.1 Hz. NMDAR EPSCs were calculated by subtracting the residual current after the application AP-5 from the dual component EPSC at +40 mV. The NMDAR/AMPAR ratio of the EPSCs was calculated as the ratio of NMDAR EPSC at +40mV and AMPAR EPSC at −60 mV. The rectification index of AMPAR EPSCs was calculated as the ratio of peak amplitude of AMPAR EPSC at +40 mV and at −60 mV. I–V relationship of NMDAR EPSCs was measured at holding potentials from −80 mV to +40 mV. The activation and deactivation kinetics of the NMDA receptor were measured at +40 mV, by fitting the rise to the single exponential equation and the decay to a double exponential equation of the form: $I(t) = I_f\exp(-t/\tau_f) + I_s\exp(-t/\tau_s)$

where I_f and I_s are the amplitudes of the fast and slow decay components, and τ_f and τ_s are their respective decay time constants. The weighted time constant was calculated as: $\tau_W = \{I_f/(I_f+I_s)\}\ \tau_f + \{I_s/(I_f+I_s)\}\ \tau_s$. Paired pulse ratios were calculated as a ratio of EPSC2 to EPSC1 separated by inter-stimulus intervals of 20, 50, 100 and 200 ms. To measure the input-output curves for PV interneurons, a theta glass electrode was place 5 cell bodies away and in the same plane as the cell. 20–30 episodes of AMPAR EPSCs to incremental stimulus strength (8 increments from 2.5 V to 20V) were measured. Spontaneous EPSCs were detected and analysed for a 700 msec period beginning 100 msec after afferent stimulation to evoke an AMPAR EPSC from recordings during the pre-drug baseline of the pharmacology experiments. Membrane properties of PV cells were measured by injecting square step current injections (500 ms) into the cells held at their resting membrane potentials. For pharmacological experiments, paired pulse AMPAR EPSCs were evoked with an ISI of 20 ms at 0.1 Hz. Drugs were applied following a 10 min baseline. For current clamp recordings, $CsMeSO_4$ in the internal solution was replaced with $KMeSO_4$. Spike frequency adaptation was measured for spikes 1–8 at rheobase. The afterhyperpolarization potential was measured as the peak hyperpolarization after the 1st spike in the train at rheobase. To evoke spiking in PV cells in current clamp, a theta glass stimulator was placed in the oriens layer and stimulation intensity was increased to the minimal necessary level to produce spiking in two consecutive stimulations given 50 ms apart. The same stimulation intensity was used during the prolonged stimulation trains. CA1 pyramidal cells (closer to oriens) were held at −60 mV in current clamp for EPSP-IPSP integration experiments and PSPs were evoked by a theta glass electrode placed in the CA1 oriens-alveus layer.

Sharp wave ripple oscillations (SWRs) were recorded from 450 μm coronal sections of the hippocampus using a 4–5 MΩ pipette filled with aCSF. To induce SWRs, the slices were perfused with a modified aCSF containing 8.5 mM potassium at a flow rate of 10 ml/min at 32–34 C[25]. To detect SWRs, local field potentials were bandpass filtered at 100–400 Hz and smoothened with a 6-point boxcar filter. Individual events were detected using an amplitude threshold algorithm that detected peaks higher than 6 times the SD of the noise of the eventless LFP. The minimum separation between events was set to 50 ms and 200 ms of the oscillatory event was captured. The captured events were visually examined to discard false positives that had less than 2 peaks crossing the set threshold.

Statistics—All data are presented as means ± SEMs. Statistical significance was calculated between the two genotypes using unpaired two-tailed t-tests ($^*p < 0.05$). For LFP recordings, power spectrum data are presented as means ± 95% confidence level. Data distribution was assumed to be normal but this was not formally tested.

In vivo electrophysiology

Linear multielectrode arrays containing 4 channels (75 μm spacing between channels. Microprobes, Gaithersburg, MD) were stereotactically implanted in the CA1 region of the hippocampus in P60–P90 mice (n=6 PV-Cre, n=6 $NL3^{fl}$/PV-Cre). In brief, mice were anaesthetized with ketamine/xylazine, and placed in a stereotaxic frame. Craniotomies were made to allow a multielectrode array to be implanted in the left hippocampus (2 mm posterior to the bregma, 1.7 mm lateral to the midline and 2.1 mm below the brain surface

for the deepest contact). Skull screws in the frontal cortex served as reference. After 1 week of recovery and acclamation period, each mouse was tethered to a neural recording device (Alphalab SnR, Alpha Omega, Nazareth, Israel) and put in an open-field box for 1 hour, during which hippocampal signals were recorded at 22k Hz continuously, together with synchronized behavioral data (Ethovision, Noldus, Wageningen, the Netherlands). To extract information in the local field potential range, signals were down sampled offline to 1375 Hz, and segments corresponding to locomotion and paradoxical sleep were extracted. The short-time Fourier transform was used to approximate the power spectrum in time-frequency domain (window of 1 second, 50% overlap). Signal processing was performed using the MatLab software package and custom scripts. Data for theta and gamma oscillations is presented as mean ± SEM. SWRs were detected using Axograph-X analysis software. LFPs during immobility were normalized, bandpass filtered at 100–400 Hz and smoothened with a 6-point boxcar filter. Individual events were detected using an amplitude threshold algorithm that detected peaks higher than 6 SD of the noise of the eventless LFP. The minimum separation between the highest peaks in two events was set to 100 ms and 500 ms of the oscillatory event was captured. The captured events were visually examined to discard false positives that had less than 2 peaks crossing a threshold of 4 times the SD of the eventless noise.

Statistics—Power spectrum data are presented as mean ± SEM. Statistical significance was calculated between the two genotypes using unpaired two-tailed t-tests ($^{*}p < 0.05$). Data distribution was assumed to be normal but this was not formally tested.

Behavior: fear conditioning and extinction

3–4 weeks following the injection of AAV virus, 3–4 month old mice were handled daily for 3 days prior to training. On day 1 of training, individual mice were placed in a sound attenuated fear-conditioning chamber cleaned with 10% ethanol. After a 2 min exploration period, 3 context-foot shock pairings separated by 1 min intervals were delivered. The mice remained in the training chamber for another 30 seconds before being returned to home cages. From day 2 until day 5, mice were reintroduced to the fear-conditioning chamber for 5 min, twice a day with a gap of 2–3 hours between sessions. The behavior of the mice was recorded with FreezeFrame software and analyzed with FreezeView software (Colbourn Instruments, Holliston, MA). Motionless bouts lasting more than 1 second were considered as freezing. Freezing was analyzed for 30 s periods. Baseline freezing was calculated as % time freezing for the first 30 s after the mice were first introduced to the chamber on day 1. Fear learning was calculated as % time freezing during the 30 s following context-foot shock pairings. Fear retention during extinction on days 2–5 was calculated as % time freezing for the first 30s when the mice were first reintroduced into the fear-conditioning chamber. Per cent times freezing were averaged for the two sessions for each day during extinction. Mice previously injected with AAV-syn-hM4Di-mCherry were injected with 10 mg/kg clozapine-N-oxide (CNO) an hour before the start of the behavioral experiments and 12 hours thereafter for all 5 days of the behavioral procedure. Animal experiments were conducted following protocols approved by Administrative Panel on Laboratory Animal Care at Stanford University.

Reward alternation task

10–12 week old PV-Cre and NL3^{fl}/PV-Cre mice were food restricted until they reached 85% of their body weight. During the first 2 days of food restriction, they were fed only chocolate pellets that they would subsequently receive in the task and were moved to a 50–50 mixture of dry food and chocolate pellets until the end of the experimental procedure. Mice were handled for 3 days prior to habituation and during habituation mice were allowed to explore all three arms of the T-maze. Food pellets were placed in the reward cups in the two arms of the maze and were constantly replaced in the 10 min session as they were consumed. After 2 habituation sessions over 2 days, mice were given 10 trials per day. Each trial consisted of two runs, the sample run and the choice run. In the sample run a reward was placed in the reward cup at the end of an arm and mice were forced to run into this arm by blocking the other arm. Over the 10 trials, the sample arm was randomly assigned to left or right to avoid biases. At the end of the trial, mice were allowed to consume the reward and were gently placed back into the start box and the arms were wiped down with 10% EtOH while the mouse was trapped in the start box. The previously blocked door was opened so that both arms of the T-maze were open for the choice run and mice were rewarded for choosing the opposite arm from the sample run. If a mouse chose the same arm as the sample run, it was blocked in the arm for 10 s as a punishment, before being returned to the start box. 10 consecutive trials were performed in each session for 6 days. Mice were scored for the %correct choices made in each session.

Force plate actometer assays

Mice were tested for locomotor activity and stereotypical behaviors on a custom made force plate actometer as described[28]. In brief, mice were placed individually in the actometer for 20 min recording sessions. The distance travelled by the mice was calculated as the sum of distances between coordinates of the location of the center of force (COF) recorded every 0.5 s over the 20 min recording session. A low mobility bout was defined as the mouse's COF remaining within a 15 mm radius for 5 s. Stereotypy score was defined as the product of the score of head mobility and the score of lack of foot mobility during the same time interval.

Behavioral data analysis and statistics

All data were collected and analyzed blind to the genotype of mice or the virus injected. Mice were randomized into groups consisting of a mixture of control and either knockout and DREADD containing mice, or control and knockout or rescue, or control and rescue and DREADD mice. Data are presented as mean ± SEM. Repeated measures ANOVA with $\alpha = 0.05$ was used to analyze the data and statistical interference was further verified with posthoc Bonferroni tests. For forceplate actometer assays, data between the two genotypes were compared using 2-tailed student's T-test with statistical significance set to $p < 0.05$. Data distribution was assumed to be normal but this was not formally tested. No statistical methods were used to pre-determine sample sizes but our sample sizes are similar to those reported in previous publications[48].

Immunohistochemistry

PV-Cre and NL3^{fl}/PV-Cre mice injected with AAV virus were anesthetized with sodium pentobarbital 150 mg/kg and perfused transcardially with 50 ml of 4% paraformaldehyde (in 0.1 M PB, pH 7.4) 45–60 days post injection. Brains were then removed and post-fixed overnight in the same fixative at 4°C and then washed in 0.1 M PBS, after which 50 μm thick coronal sections containing the hippocampus and the frontal cortex were cut using a vibratome (Leica VT1000S). Sections were serially washed 4 times in PBS, and blocked using a blocking buffer (PBS+0.1% triton X-100 + 2% bovine serum albumin + 2% goat serum) for 30 minutes. Antibodies to parvalbumin (1:1000; Sigma-Aldrich, P3088), GluA4 (5μg/ml; Abcam, ab115322), PSD-95 (1:100; Abcam, ab13552–50) and GFP (1:1000; Abcam, ab13970) were made up separately in incubation buffers (0.1% goat serum+ 0.4% Triton X-100) and sections were incubated with the antibody in a dark room at 4°C overnight. After four 10 minute washes in PBS, sections were transferred to Alexa-488, Alexa-594 and Alexa 633 secondary antibodies accordingly in incubation buffer at room temperature in the dark for 2 hours. The sections were then washed, mounted, coverslipped and imaged using a Nikon confocal microscope. Images were processed and analyzed using Image J. To quantify the % infection of hippocampal parvalbumin neurons with AAV-DIO-NL3-GFP, we used 5–6 labelled sections from each hemisphere along the rostro-caudal axis of the hippocampus. Cell bodies labelled with parvalbumin and GFP antibodies throughout the hippocampus were visually analyzed using Image-J, and the numbers of co-labelled cells per section were averaged.

Supplementary Material

Refer to Web version on PubMed Central for supplementary material.

Acknowledgments

We thank Stephan Maxeiner for sharing NL3^{fl} mice, Scarlett Fang, Seyedeh Atiyeh Afjei for help with stereotaxic injections, Karen Lee for help with *in vivo* recording experiments and Salome Botelho for help with biochemical assays. This work was supported by grants from NIH (P50MH086403 to R.C.M. and T.C.S.) and the Simons Foundation Autism Research Initiative (to T.C.S.). Correspondence and requests for materials should be addressed to: R. C. Malenka (malenka@stanford.edu) or T.C. Südhof (tcs1@stanford.edu).

References

1. Buzsaki G, Anastassiou CA, Koch C. The origin of extracellular fields and currents--EEG, ECoG, LFP and spikes. Nat Rev Neurosci. 2012; 13:407–420. [PubMed: 22595786]
2. Gulyas AI, Freund TT. Generation of physiological and pathological high frequency oscillations: the role of perisomatic inhibition in sharp-wave ripple and interictal spike generation. Curr Opin Neurobiol. 2015; 31:26–32. [PubMed: 25128735]
3. Korotkova T, Fuchs EC, Ponomarenko A, von Engelhardt J, Monyer H. NMDA receptor ablation on parvalbumin-positive interneurons impairs hippocampal synchrony, spatial representations, and working memory. Neuron. 2010; 68:557–569. [PubMed: 21040854]
4. Marin O. Interneuron dysfunction in psychiatric disorders. Nat Rev Neurosci. 2012; 13:107–120. [PubMed: 22251963]
5. Sah P, Hestrin S, Nicoll RA. Properties of excitatory postsynaptic currents recorded in vitro from rat hippocampal interneurones. J Physiol (Lond). 1990; 430:605–616. [PubMed: 1982315]

6. Geiger JR, et al. Relative abundance of subunit mRNAs determines gating and Ca2+ permeability of AMPA receptors in principal neurons and interneurons in rat CNS. Neuron. 1995; 15:193–204. [PubMed: 7619522]
7. Lamsa KP, Heeroma JH, Somogyi P, Rusakov DA, Kullmann DM. Anti-Hebbian long-term potentiation in the hippocampal feedback inhibitory circuit. Science. 2007; 315:1262–1266. [PubMed: 17332410]
8. Jamain S, et al. Mutations of the X-linked genes encoding neuroligins NLG3 and NLG4 are associated with autism. Nat Genetics. 2003; 34:27–29. [PubMed: 12669065]
9. Sudhof TC. Neuroligins and neurexins link synaptic function to cognitive disease. Nature. 2008; 455:903–911. [PubMed: 18923512]
10. Rothwell PE, et al. Autism-associated neuroligin-3 mutations commonly impair striatal circuits to boost repetitive behaviors. Cell. 2014; 158:198–212. [PubMed: 24995986]
11. Isaac JT, Ashby MC, McBain CJ. The role of the GluR2 subunit in AMPA receptor function and synaptic plasticity. Neuron. 2007; 54:859–871. [PubMed: 17582328]
12. Nyiri G, Stephenson FA, Freund TF, Somogyi P. Large variability in synaptic N-methyl-D-aspartate receptor density on interneurons and a comparison with pyramidal-cell spines in the rat hippocampus. Neurosci. 2003; 119:347–363.
13. Zucker RS, Regehr WG. Short-term synaptic plasticity. Annu Rev Physiol. 2002; 64:355–405. [PubMed: 11826273]
14. Kavalali ET. The mechanisms and functions of spontaneous neurotransmitter release. Nat Rev Neurosci. 2015; 16:5–16. [PubMed: 25524119]
15. Hessler NA, Shrike AM, Malinow R. The probability of transmitter release at a mammalian central synapse. Nature. 1993; 366:569– 572. [PubMed: 7902955]
16. Foldy C, Malenka RC, Sudhof TC. Autism-associated neuroligin-3 mutations commonly disrupt tonic endocannabinoid signaling. Neuron. 2013; 78:498–509. [PubMed: 23583622]
17. Anderson GR, et al. beta-Neurexins Control Neural Circuits by Regulating Synaptic Endocannabinoid Signaling. Cell. 2015; 162:593–606. [PubMed: 26213384]
18. Gibson HE, Edwards JG, Page RS, Van Hook MJ, Kauer JA. TRPV1 channels mediate long-term depression at synapses on hippocampal interneurons. Neuron. 2008; 57:746–759. [PubMed: 18341994]
19. Thompson SM, Capogna M, Scanziani M. Presynaptic inhibition in the hippocampus. Tr Neurosci. 1993; 16:222–227.
20. Shigemoto R, et al. Target-cell-specific concentration of a metabotropic glutamate receptor in the presynaptic active zone. Nature. 1996; 381:523–525. [PubMed: 8632825]
21. Allen K, Monyer H. Interneuron control of hippocampal oscillations. Curr Opin Neurobiol. 2015; 31:81–87. [PubMed: 25240150]
22. Stark E, et al. Pyramidal cell-interneuron interactions underlie hippocampal ripple oscillations. Neuron. 2014; 83:467–480. [PubMed: 25033186]
23. Jadhav SP, Kemere C, German PW, Frank LM. Awake hippocampal sharp-wave ripples support spatial memory. Science. 2012; 336:1454–1458. [PubMed: 22555434]
24. Girardeau G, Benchenane K, Wiener SI, Buzsaki G, Zugaro MB. Selective suppression of hippocampal ripples impairs spatial memory. Nat Neurosci. 2009; 12:1222–1223. [PubMed: 19749750]
25. Dzhala VI, Staley KJ. Mechanisms of fast ripples in the hippocampus. J Neurosci. 2004; 24:8896–8906. [PubMed: 15470156]
26. Donato F, Rompani SB, Caroni P. Parvalbumin-expressing basket-cell network plasticity induced by experience regulates adult learning. Nature. 2013; 504:272–276. [PubMed: 24336286]
27. Xu W, et al. Distinct neuronal coding schemes in memory revealed by selective erasure of fast synchronous synaptic transmission. Neuron. 2012; 73:990–1001. [PubMed: 22405208]
28. Fowler SC, et al. A force-plate actometer for quantitating rodent behaviors: illustrative data on locomotion, rotation, spatial patterning, stereotypies, and tremor. J Neurosci Meth. 2001; 107:107–124.

29. Chubykin AA, et al. Activity-dependent validation of excitatory versus inhibitory synapses by neuroligin-1 versus neuroligin-2. Neuron. 2007; 54:919–931. [PubMed: 17582332]
30. Blundell J, et al. Neuroligin-1 deletion results in impaired spatial memory and increased repetitive behavior. J Neurosci. 2010; 30:2115–2129. [PubMed: 20147539]
31. Jung SY, et al. Input-specific synaptic plasticity in the amygdala is regulated by neuroligin-1 via postsynaptic NMDA receptors. Proc Natl Acad Sci USA. 2010; 107:4710–4715. [PubMed: 20176955]
32. Losonczy A, Somogyi P, Nusser Z. Reduction of excitatory postsynaptic responses by persistently active metabotropic glutamate receptors in the hippocampus. J Neurophysiol. 2003; 89:1910–1919. [PubMed: 12686572]
33. Scanziani M, Gahwiler BH, Charpak S. Target cell-specific modulation of transmitter release at terminals from a single axon. Proc Natl Acad Sci USA. 1998; 95:12004–12009. [PubMed: 9751780]
34. Losonczy A, Zhang L, Shigemoto R, Somogyi P, Nusser Z. Cell type dependence and variability in the short-term plasticity of EPSCs in identified mouse hippocampal interneurones. J Physiol (Lond). 2002; 542:193–210. [PubMed: 12096061]
35. Ferraguti F, et al. Metabotropic glutamate receptor 8-expressing nerve terminals target subsets of GABAergic neurons in the hippocampus. J Neurosci. 2005; 25:10520–10536. [PubMed: 16280590]
36. Pelkey KA, Topolnik L, Yuan XQ, Lacaille JC, McBain CJ. State-dependent cAMP sensitivity of presynaptic function underlies metaplasticity in a hippocampal feedforward inhibitory circuit. Neuron. 2008; 60:980–987. [PubMed: 19109906]
37. Suh YH, et al. Corequirement of PICK1 binding and PKC phosphorylation for stable surface expression of the metabotropic glutamate receptor mGluR7. Neuron. 2008; 58:736–748. [PubMed: 18549785]
38. Zhang CS, et al. Knock-in mice lacking the PDZ-ligand motif of mGluR7a show impaired PKC-dependent autoinhibition of glutamate release, spatial working memory deficits, and increased susceptibility to pentylenetetrazol. J Neurosci. 2008; 28:8604–8614. [PubMed: 18716219]
39. Schlingloff D, Kali S, Freund TF, Hajos N, Gulyas AI. Mechanisms of sharp wave initiation and ripple generation. J Neurosci. 2014; 34:11385–11398. [PubMed: 25143618]
40. Forro T, Valenti O, Lasztoczi B, Klausberger T. Temporal organization of GABAergic interneurons in the intermediate CA1 hippocampus during network oscillations. Cerebral Cortex. 2015; 25:1228–1240. [PubMed: 24275828]
41. Carlen M, et al. A critical role for NMDA receptors in parvalbumin interneurons for gamma rhythm induction and behavior. Mol Psychiatry. 2012; 17:537–548. [PubMed: 21468034]
42. Zhang B, et al. Neuroligins sculpt cerebellar purkinje-cell circuits by differential control of distinct classes of synapses. Neuron. 2015; 87:781–796. [PubMed: 26291161]
43. Aoto J, Foldy C, Ilcus SM, Tabuchi K, Sudhof TC. Distinct circuit-dependent functions of presynaptic neurexin-3 at GABAergic and glutamatergic synapses. Nat Neurosci. 2015; 18:997–1007. [PubMed: 26030848]
44. Liang J, et al. Conditional neuroligin-2 knockout in adult medial prefrontal cortex links chronic changes in synaptic inhibition to cognitive impairments. Mol Psychiatry. 2015; 20:850–859. [PubMed: 25824299]
45. Etherton M, et al. Autism-linked neuroligin-3 R451C mutation differentially alters hippocampal and cortical synaptic function. Proc Natl Acad Sci USA. 2011; 108:13764–13769. [PubMed: 21808020]
46. Tabuchi K, et al. A neuroligin-3 mutation implicated in autism increases inhibitory synaptic transmission in mice. Science. 2007; 318:71–76. [PubMed: 17823315]
47. Jiang M, Polepalli J, Chen LY, Zhang B, Sudhof TC, Malenka RC. Conditional ablation of neuroligin-1 in CA1 pyramidal neurons blocks LTP by a cell-autonomous NMDAR receptor independent mecnahism. Mol Psychiatry. 2016; 80
48. Clem RL, Huganir RL. Calcium-permeable AMPA receptor dynamics mediate fear memory erasure. Science. 2010; 330:1108–1112. [PubMed: 21030604]

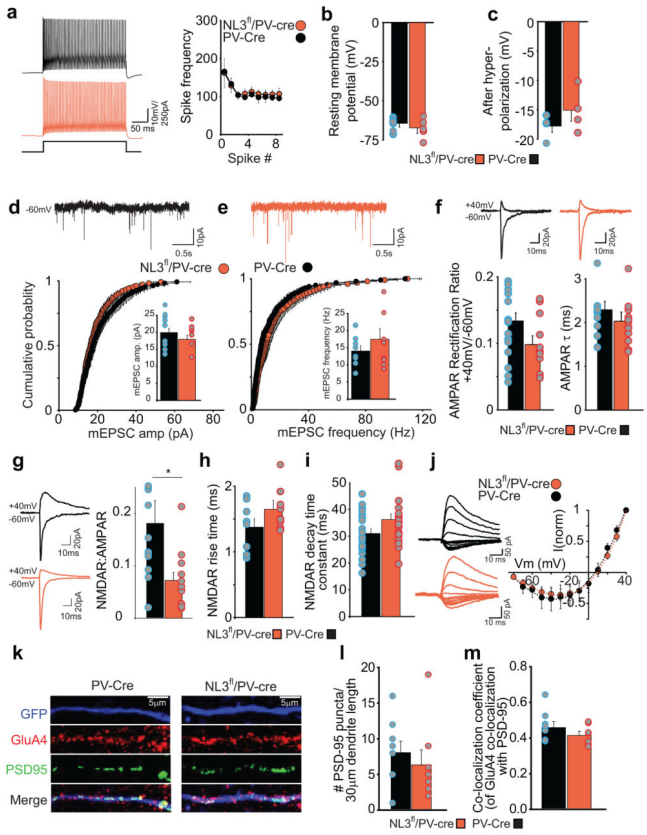

Figure 1.

NL3 deletion reduces NMDA receptor-mediated EPSCs in hippocampal PV interneurons. (**a)** Firing properties of CA1 PV interneurons in wild type PV-Cre and NL3^{fl}/PV-Cre mice. Sample traces in response to twice threshold current injection (left). Spike frequency as a function of spike number (right) is unchanged by NL3 deletion (Frequency at spikes 4–8: PV-Cre, 111 ± 10 Hz, n=6 cells; NL3^{fl}/PV-Cre, 115 ± 10 Hz, n=6 cells). (**b)** Resting membrane potential of PV interneurons is unchanged by NL3 deletion (PV-Cre, −64 ± 2 mV, n=6 cells; NL3^{fl}/PV-Cre, −67 ± 3 mV, n=6 cells). (**c)** Amplitude of fast afterhyperpolarizing potential is unchanged by NL3 deletion (PV-Cre, 18 ± 1 mV, n=4 cells; NL3^{fl}/PV-Cre, 15± 2 mV, n=4 cells). (**d–e)** (top) sample traces showing mEPSCs. (bottom) cumulative distribution plot for AMPAR mEPSC amplitudes (**d**) and frequency (**e**) showing no change due to NL3 deletion ($p > 0.05$, KS test for both amplitude and frequency). Inset shows average mEPSC amplitudes (**d**) (PV-Cre, 21 ± 2 pA, n=9 cells; NL3^{fl}/PV-Cre, 19 ± 2 pA, n= 8 cells; $p > 0.05$) and mEPSC frequency (**e**) (PV-Cre, 14 ± 2 Hz, n = 9 cells; NL3^{fl}/PV-Cre, 17 ± 3 Hz, n= 8 cells; $p > 0.05$). (**f**) (top) sample average traces showing evoked AMPAR EPSCs at −70 and +40 mV. (bottom) rectification ratio (left) measured as a ratio of peak AMPAR current at +40 mV and −60 mV is unchanged by NL3 deletion (PV-Cre, 0.13 ± 0.1, n = 19 cells; NL3^{fl}/PV-Cre, 0.09 ± 0.02, n= 11 cells; $p > 0.05$). AMPAR EPSC decay kinetics (right) fitted with a single exponential fit are unchanged by NL3 deletion (PV-Cre, 2.3 ± 0.2, n = 12 cells; NL3^{fl}/PV-Cre, 2.0 ± 0.2, n= 11 cells; $p > 0.05$). (**g**) Representative traces of AMPAR EPSCs recorded at −60 mV and dual component EPSC at +40 mV (left). NMDAR/ AMPAR ratio (right) is reduced by NL3 deletion (PV-Cre, 0.18 ± 0.1, n = 12 cells;

NL3^{fl}/PV-Cre, 0.07 ± 0.1, n = 12 cells; p < 0.05). (**h**) NMDAR EPSC rise time is unchanged by NL3 deletion (NL3^{fl}/PV-Cre, 1.37 ± 0.10 ms, n = 8 cells; PV-Cre, 1.64 ± 0.15 ms, n = 10 cells; p>0.05). (**i**) Weighted decay time constants for NMDAR EPSCs are unchanged by NL3 deletion (NL3^{fl}/PV-Cre, 31.0 ± 1.8 ms, n = 20 cells; PV-Cre, 36.2 ± 2.1 ms, n = 22 cells; p>0.05). (**j**) I–V relationship of NMDAR EPSCs is unchanged by NL3 deletion. **k,** Representative images from dendrites (30 μm) of hippocampal PV-Cre (left) and NL3^{fl}/PV-Cre neurons infected with AAV-DIO-GFP and immunolabeled for GFP (top), GluA4, PSD-95 (middle) with merged images (bottom). **l**, Bar graph quantifying the number of PSD-95 puncta per 30 μm of the dendrite (PV-Cre 8.2 ± 1.5, n = 9; NL3^{fl}/PV-Cre, 6.5 ± 1.9, n = 8; p > 0.1). **m**, Bar graph showing the co-localization of GluA4 and PSD-95 puncta (Co-localization coefficient in PV-Cre 0.46 ± 0.02, n = 9; NL3^{fl}/PV-Cre, 0.42 ± 0.02, n = 8; p > 0.1).

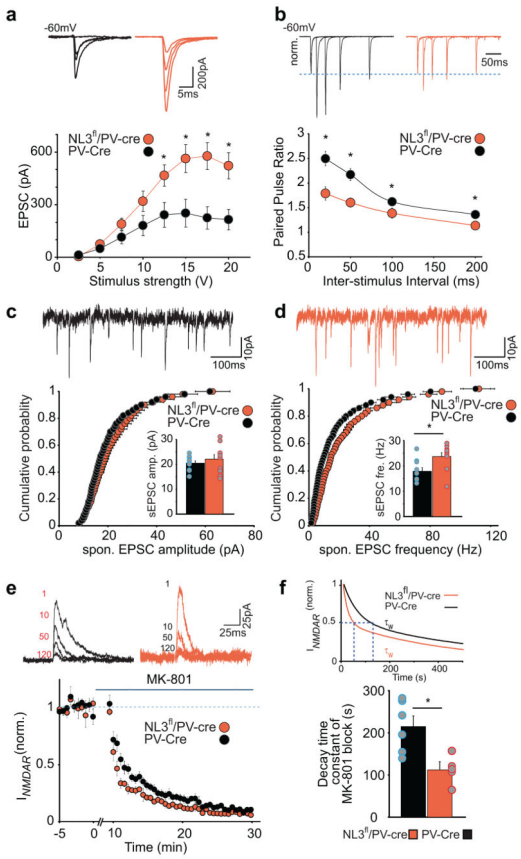

Figure 2.

Deletion of postsynaptic NL3 causes an increase in glutamate release probability at synapses on PV interneurons. (**a**) Representative traces (top) and plot (bottom) show increased input-output relationship of AMPAR EPSCs in cells lacking NL3 for incremental stimulation intensities (in V) 2.5, 5,7.5,10, 12.5, 15, 17.5 and 20 (PV-Cre, 12.3 ± 7.1, 49.8 ± 21.6, 114.9 ± 34.7, 181.1 ± 56.5, 241.3 ± 68.8, 252.4 ± 78.5, 224.6 ± 62.1, 215.1 ± 56.4, n = 7 cells; $NL3^{fl}$/PV-Cre, 4.9 ± 2.0, 74.5 ± 12.5, 189.7 ± 32.5, 319.8 ± 55.8, 446.8 ± 59.7, 563.4 ± 77.6, 576.5 ± 75.3, 521.2 ± 72.7, n = 7 cells; p= 0.33, 0.34, 0.14, 0.10, 0.02, 0.01, 0.003, 0.006 for each stimulus intensity) (**b**) Representative average traces (top) and plot (bottom) show reduced paired pulse ratios at inter-stimulus intervals of 20, 50, 100 and 200 ms in cells lacking NL3 (PV-Cre, 2.5 ± 0.1, 2.2 ± 0.1, 1.6 ± 0.1, 1.4 ± 0.1, n = 11 cells; $NL3^{fl}$/PV-Cre, 1.8 ± 0.1, 1.6 ± 0.1, 1.4 ± 0.1, 1.1 ± 0.1, n = 12 cells; p < 0.01, 0.01, 0.05, 0.05 for each inter-stimulus interval). (**c–d)** (top) sample traces showing spontaneous EPSCs. (bottom) cumulative distribution plot for AMPAR sEPSC amplitudes (**c**) and frequency (**d**) showing unchanged sEPSC amplitude and increased sEPSC frequency as a result of NL3 deletion (p = 0.3, Mann-Whitney test for amplitude, p = 0.03 Mann-Whitney test for frequency). Inset shows average sEPSC amplitudes (**c**) (PV-Cre, 20.5 ± 0.9 pA, n= 10 cells; $NL3^{fl}$/PV-Cre, 22.1 ± 1.8 pA, n= 10 cells) and mEPSC frequency (**d**) (PV-Cre, 17.9 ± 1.4 Hz, n = 10 cells; $NL3^{fl}$/PV-Cre, 23.6 ± 1.6 Hz, n= 10 cells) (**e**) Representative traces (top) for 1^{st}, 10^{th}, 50^{th} and 120^{th} NMDAR EPSC at +40 mV following 10 min wash-in of 40 μM MK-801 and summary time course (bottom) showing an accelerated block of NMDAR EPSC in cells

lacking NL3. (**f**) Double exponential fit for the weighted decay time constant of MK-801 block (top) in PV-Cre and $NL3^{fl}$/PV-Cre cells and summary bar graph with mean decay time constant of MK 801 block (bottom) (PV-Cre, τ_w = 215 ± 25 ms, n = 6 cells; NL3fl/PV-Cre, 112 ± 19 ms, n = 5 cells; $p < 0.05$).

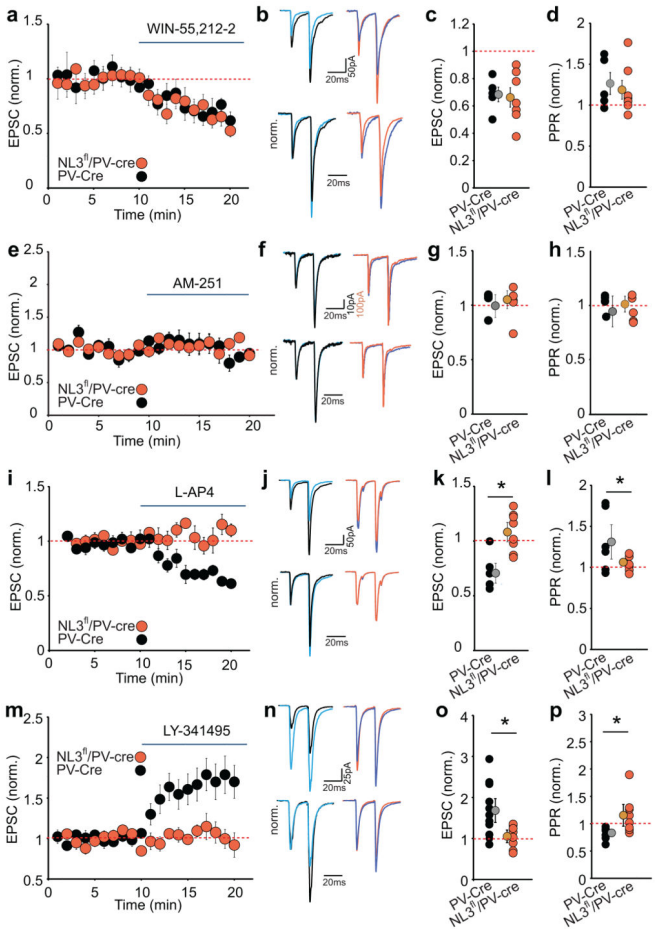

Figure 3.

Increase in glutamate release caused by NL3 deletion at synapses on PV interneurons is due to loss of Group III mGluR-mediated presynaptic inhibition. (**a–d**) The depression of excitatory synaptic transmission in PV interneurons by the CB1 receptor agonist WIN 55,212-2 (5 μM) is not affected by NL3 deletion. Time course of normalized AMPAR EPSCs during application of WIN 55212-2 (**a**) and sample EPSCs in response to paired pulse stimulation before and after WIN 55212-2 application (**b**) in PV-Cre (before-black, after-blue) and NL3^{fl}/PV-Cre (before-orange, after-blue) neurons. Summary plot of normalized EPSC changes due to WIN 55212-2 (**c**) and normalized PPR changes (**d**) in individual cells (PV-Cre, 0.68 ± 0.05, 1.3 ± 0.1, n=5; NL3^{fl}/PV-Cre, 0.66 ± 0.07, 1.2 ± 0.1 n=7). **e–h**. Same as a-d but for effect of CB1-R antagonist AM251 (10 μM). Representative EPSCs (**f**) before and after AM251 for PV-Cre cell (before-black, after-blue) and NL3^{fl}/PV-Cre (before-orange, after-blue). Individual normalized EPSC (**g**) and PPR (**h**) after AM251 application (PV-Cre, 1.0 ± 0.1, 0.9 ± 0.1, n = 5; NL3^{fl}/PV-Cre, 1.05 ± 0.08, 1.07 ± 0.1 n = 5; p > 0.1). **i–l**. Same as a-d but for effect of Group III mGluR agonist L-AP4 (10 μM). Representative EPSCs (**j**) before and after L-AP4 for PV-Cre cell (before-black, after-blue) and NL3^{fl}/PV-Cre (before-orange, after-blue). Individual normalized EPSC (**k**) and PPR (**l**) changes caused by L-AP4 (PV-Cre, 0.7 ± 0.1, 1.3 ± 0.1, n = 6; NL3^{fl}/PV-Cre, 1.1 ± 0.1, 1.0 ± 0.05, n = 8; *p < 0.05). **m–p**, Same as i-l but for application of Group III mGluR

antagonist LY341414 (1 μM) showing changes in EPSC and PPR in PV-Cre cells (1.7 ± 0.2, 0.9 ± 0.03, n = 11) and $NL3^{fl}$/PV-Cre cells (1.0 ± 0.1, 1.1 ± 0.1, n = 8; *p < 0.05).

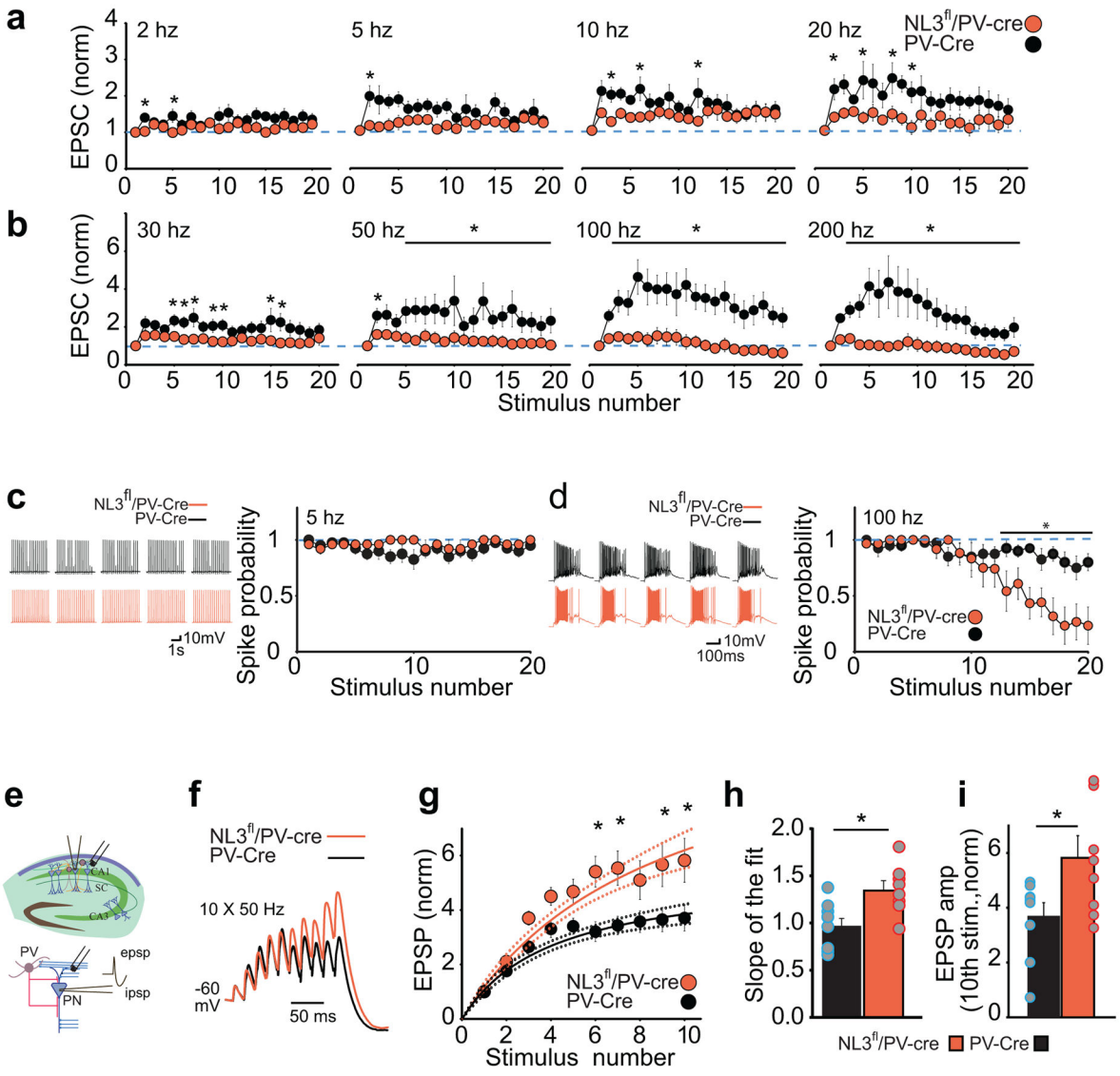

Figure 4.

Changes in synaptic responses to repetitive stimulation as a result of NL3 deletion from PV interneurons. **a–b,** Normalized EPSC amplitudes in response to stimulation trains applied at increasing frequencies. Response in PV-Cre and NL3^{fl}/PV-Cre cells for 2 Hz, 5 Hz, 10 Hz and 20 Hz stimulation (**a**) and for 30 Hz, 50 Hz, 100 Hz, and 200 Hz stimulation (**b**) (PV-Cre, n=10 cells; NL3^{fl}/PV-Cre, n=12 cells; *p < 0.05, posthoc Bonferroni test). **c–d,** The probability of generating spikes in response to prolonged stimulus trains in PV-Cre and NL3^{fl}/PV-Cre cells for 5 hz (**c**) and 100 hz (**d**) trains. Representative traces (left) and summary graphs (right) are shown. Spikes were reliably evoked at 5 Hz in both PV-Cre (n = 8 cells) and NL3^{fl}/PV-Cre cells (n = 5) (p > 0.99, posthoc Bonferroni test), but showed increased attenuation as the train progresses at 100 Hz in NL3^{fl}/PV-Cre (*p < 0.05, posthoc Bonferroni test). **e**, Schematic of experimental setup for recording synaptic integration in CA1 pyramidal neurons in the absence of $GABA_AR$ blockers. Stimulating electrode was placed in str. oriens to evoke monosynaptic EPSPs and disynaptic IPSPs. **f**, Representative

traces of synaptic potentials in CA1 pyramidal cells from PV-Cre and $NL3^{fl}$/PV-Cre held at −60 mV during 50 Hz stimulation. **g,** Summary graphs showing normalized EPSP summation as function of stimulation number and the corresponding fitted curve with 95% confidence limits (*$p < 0.05$, posthoc Bonferroni test). **h,** Bar graph showing the slope of the EPSP summation as a function of the stimulation number (PV-Cre, 0.98 ± 0.08, n = 9 cells; $NL3^{fl}$/PV-Cre, 1.36 ± 0.09, n = 8 cells, *$p < 0.001$ T-test) **i**, Bar graph showing normalized EPSP amplitude after the 10^{th} stimulation (PV-Cre, 3.7 ± 0.5, n = 9 cells; $NL3^{fl}$/PV-Cre, 5.8 ± 0.8, n = 8 cells, *$p < 0.05$ T-test).

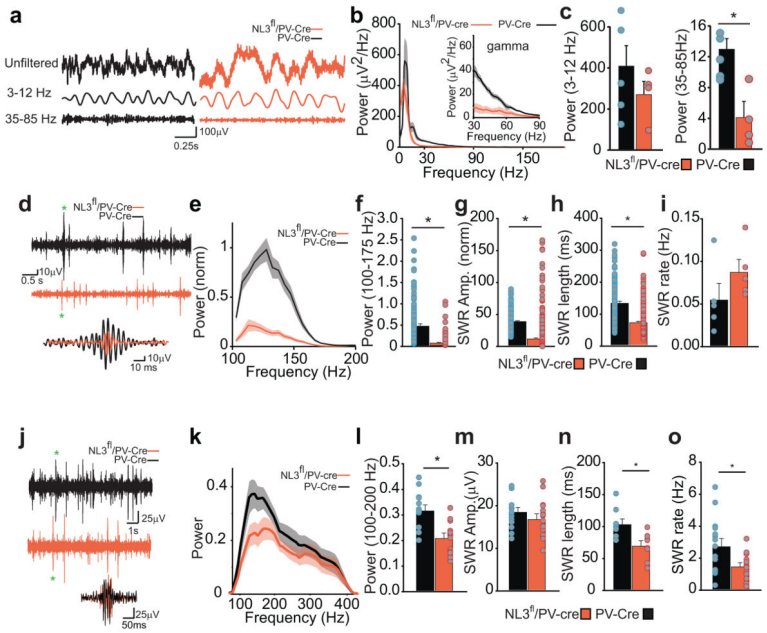

Figure 5.

Changes in hippocampal network activity as a result of NL3 deletion from PV interneurons. **a,** Representative unfiltered *in vivo* LFP traces (top), 3–12 Hz band passed filtered LFP (middle) and 35–85 Hz band pass filtered LFP (bottom) recorded in the CA1 pyramidal cell layer from PV-Cre (left) and NL3^{fl}/PV-Cre (right) mice. **b**, Normalized power spectrum of the band pass filtered LFP (3–200 Hz) from PV-Cre (n = 5) and NL3^{fl}/PV-Cre (n = 4) mice (left). Power spectra in the 30–90 Hz range are presented in the inset to emphasize the reduction in gamma power in NL3^{fl}/PV-Cre mice. **c**, (left) Bar graph quantifying the theta power (PV-Cre, 408.6 ± 93.2, n = 5; NL3^{fl}/PV-Cre, 248 ± 53.9, n = 4; p > 0.1), and (right) bar graph showing a reduction in the power of the gamma in NL3^{fl}/PV-Cre mice (PV-Cre, 12.9 ± 1.4, n = 5; NL3^{fl}/PV-Cre, 4.1 ± 2.1, n = 4; *p < 0.05) (right).**d–i,** Sharp wave ripples are dramatically reduced in NL3^{fl}/PV-Cre mice. **d**, representative 100–300 Hz band passed filtered signals showing SWRs from PV-Cre and NL3fl/PV-Cre mice and two representative SWRs from PV-Cre and NL3fl/PV-Cre overlapped. **e**, Normalized power spectrum of the captured SWRs shows a reduction in the power of the SWR in NL3^{fl}/PV-Cre mice. **f**, Bar graph quantifying the normalized power of the SWRs (PV-Cre, 0.5 ± 0.06, n = 182 events; NL3^{fl}/PV-Cre, 0.1 ± 0.02, n = 352 events; *p < 0.005). **g**, Normalized average amplitude of the SWR is reduced in NL3^{fl}/PV-Cre mice (PV-Cre, 40.5 ± 1.3, n = 182 events; NL3^{fl}/PV-Cre, 13.2 ± 1.5, n = 352 events; *p < 0.005). **h**, Length of SWR is reduced in NL3^{fl}/PV-Cre mice (PV-Cre, 135 ± 4.3 ms, n = 182 events; NL3^{fl}/PV-Cre, 75.5 ± 2.2ms, n = 352 events; *p < 0.005). **i**, Rate of SWR incidence is not significantly altered in NL3^{fl}/PV-Cre mice (PV-Cre, 0.56 ± 0.02 Hz, n = 5 mice; NL3^{fl}/PV-Cre, 0.088 ± 0.01, n = 4 mice; p = 0.06). **j,** Representative 100–400 Hz band passed filtered LFP traces containing sharp wave ripples (SWR). **k**, LFPs in NL3^{fl}/PV-Cre slices show reduced power in 100–200 Hz bandwidth. Data are represented as mean ± 95% confidence limits **l**, Bar graph showing average LFP power in the 100–200 Hz range (in PV-Cre, 0.32 ± 0.02 μV^2/Hz, n = 13 slices; NL3^{fl}/PV-Cre, 0.21 ± 0.02 μV^2/Hz, n = 13 slices; * p < 0.05, T-test). **m**, Amplitude of SWRs (PV-Cre,

18.7 ± 1.0 μV; NL3^{fl}/PV-Cre, 17.0 ± 1.1 μV; $p > 0.05$). **n**, Length of SWRs are reduced in NL3^{fl}/PV-Cre mice (PV-Cre, 104.2 ± 8.5 ms, n = 10 slices; NL3^{fl}/PV-Cre, 69.9 ± 8.7 ms, n = 10 slices; *$p < 0.05$). **o**, Rate of SWRs are decreased in NL3^{fl}/PV-Cre mice (PV-Cre, 2.8 ± 0.4 Hz; NL3^{fl}/PV-Cre, 1.5 ± 0.2 Hz; * $p < 0.05$, T-test).

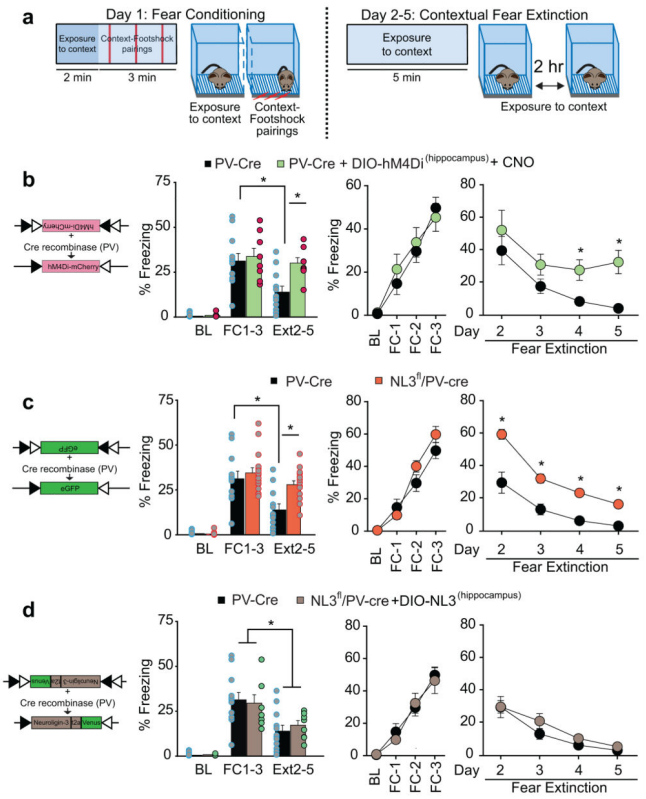

Figure 6.

Deletion of NL3 from CA1 PV interneurons compromises contextual fear extinction. **a**, Schematic representation of fear conditioning and extinction protocols. **b**, Schematic representation of DIO-hM4D1-mCherry construct (left). Bar graph shows % time freezing for control PV-Cre (all of which received injections of AAV expressing Cre-dependent eGFP) and PV-Cre mice expressing hM4Di in hippocampal PV cells treated with CNO (10 mg/kg). Baseline (BL) habituation to context (PV-Cre mice, 0.7 ± 0.4%, n = 12; hM4Di expressing mice, 1.0 ± 0.3%, n = 8); average % time freezing for fear conditioning bouts 1–3 (FC1-3 PV-Cre mice, 31.3 ± 5.5%; hM4Di injected mice 33.8 ± 5.8%), and average % time freezing during Days 2–5 of extinction (Ext2-5 PV-Cre mice, 14.0 ± 4.1%; hM4Di injected mice, 29.5 ± 6.2%, *p < 0.05, posthoc Bonferroni test). Two right graphs show time course of % time freezing during BL, FC bouts 1–3, and 4 days of fear extinction. **c**, Schematic representation of AAV-DIO-eGFP construct injected into $NL3^{fl}$/PV-Cre and PV-Cre mouse hippocampus (*left*). Graphs same as b. (Data for control PV-Cre mice are the same as shown in b.) (Bar graph: BL $NL3^{fl}$/PV-Cre, 0.6 ± 0.2%, n = 16; FC1-3 $NL3^{fl}$/PV-Cre, 34.6 ± 3.4%; Ext2-5 $NL3^{fl}$/PV-Cre, 27.9 ± 3.1; *p < 0.05, posthoc Bonferroni test). **d**, Schematic representation of AAV-DIO-NL3-t2a-Venus construct injected into $NL3^{fl}$/PV-Cre mouse hippocampus *(left).* Graphs same as b. (Data for control PV-Cre mice are the same as shown in b.) (Bar graph: BL $NL3^{fl}$/PV-Cre rescue, 0.9 ± 0.2%, n = 8 mice; FC1-3 $NL3^{fl}$/PV-Cre rescue, 29.5 ± 5.2%; Ext2-5 $NL3^{fl}$/PV-Cre rescue, 17.2 ± 3.5%; *p < 0.05, posthoc Bonferroni test).